ORIGINAL RESEARCH ARTICLE

Interaction Between Oxide Inclusions and Low-Density Steel During Heat Treatment

WEISHENG WANG, HANGYU ZHU, JIE ZHOU, MINGMING SONG, and LANQING WANG

A novel liquid-metal-suction (LMS) method was performed to prepare diffusion couple specimens. The Al_2O_3/steel and MgO/steel interface characteristics were investigated after heat treatment at 1373 K (1100 °C) for 10 hours using an electron probe microanalyzer (EPMA) and scanning electron microscopy (SEM). The results indicated that the bulk oxide and steel combined tightly. After heat treatment, the diffusion of oxygen from the oxide to the steel matrix resulted in the formation of oxide particles in the particle precipitation zone (PPZ) on the steel side. At the Al_2O_3/steel interface, fine Al_2O_3 and coarse Al_2O_3 were observed in the PPZ after heat treatment. At the MgO/steel interface, $MgO{\cdot}Al_2O_3$ (MA) spinel particles and dendritic Al_2O_3 were observed in the PPZ, and a thin MA spinel layer was detected on the bulk MgO side. After heating at 1373 K (1100 °C), the typical non-metallic inclusions (NMIs) in the low-density samples included AlN, MnS, AlN–MnS, and a small amount of Al_2O_3–MnS, whereas MnS-containing NMIs became spherical or near-spherical, and the number of fine AlN inclusions increased. In addition, the Mn diffusion from the steel matrix to the interface was revealed based on Fick's second law, and the Mn contents detected through EPMA analysis after heat treatment were consistent with the theoretical calculation.

https://doi.org/10.1007/s11663-022-02580-9

I. INTRODUCTION

LOW-DENSITY steels (also known as lightweight steels) for the transportation industry and military vehicles have attracted increasing attention due to their combined lightweight reduction, excellent strength, and toughness.[1–3] The high Mn and Al content in low-density steel leads to a challenge for the control of non-metallic inclusions (NMIs) during the smelting process. It is well known that NMIs have remarkable influences on the properties of steel.[4–6] Some researchers[7–10] have reported that the main NMIs in low-density steels are Al_2O_3, AlN, $MgO{\cdot}Al_2O_3$, MnS, and the relevant complex inclusions. The formation of NMIs is closely related to the chemical composition (oxygen, nitrogen, sulfur, *etc.*), refining slag, refractory, and the smelting process. Generally, the control of NMIs was focused on the refining and casting process, which has been widely investigated.

In recent years, the evolution of NMIs during heat treatment has attracted more attention. Ren *et al.*[11] investigated the transformation behavior of oxide inclusions in 304 stainless steel heated from 1273 K to 1473 K (1000 °C to 1200 °C) and found that the addition of Cr into the steel matrix could transform $MnO–SiO_2$ to $MnO–Cr_2O_3$. Yang *et al.*[12] concluded that the formation of $MnO–Cr_2O_3$ particles was not only due to interfacial chemical reactions but also to Ostwald ripening. Kim *et al.*[13,14] investigated the solid reaction between $MnO–SiO_2–FeO$ oxide and Fe-Mn-Si steel by diffusion couple experiments. They pointed out that oxide particles precipitated in the particle-precipitated zone (PPZ), and iron particles containing Si and Mn precipitated in the bulk oxides. It was confirmed that the diffusion of S can suppress the diffusion of O and then prevent the solid reaction between bulk oxide and steel during heat treatment.[15,16] Zhang *et al.*[17] reported that the PPZ width was controlled by the decomposition of FeO in bulk oxide.

For oxides without FeO, there was still a solid reaction between oxides and steel during heat treatment. Kim *et al.*[18] studied the diffusion of elements and change in composition between oxide inclusions and steel and pointed out that Mn diffused into the steel

WEISHENG WANG, HANGYU ZHU, and MINGMING SONG are with the State Key Laboratory of Refractories and Metallurgy, Wuhan University of Science and Technology, Wuhan, Hubei 430081, P.R. China. Contact e-mail: zhuhy@wust.edu.cn JIE ZHOU and LANQING WANG are with the Key Laboratory for Ferrous Metallurgy and Resources Utilization of Ministry of Education, Wuhan University of Science and Technology, Wuhan, Hubei 430081, P.R. China.

Manuscript submitted April 11, 2022; accepted June 1, 2022.
Article published online June 27, 2022.

from the oxide, while the diffusion of Si occurred in the opposite direction. The driving force for the diffusion of Mn and Si was subject to the activities of MnO and SiO_2 in the oxide. Gan *et al.*[19] reported that $MgO–Al_2O_3–SiO_2–CaO$ oxide was transformed to $Al_2O_3–TiO_x–Cr_2O_3–MnO$ oxide due to the solid reaction between Cr, Mn, Ti in the steel and SiO_2 in oxides. Due to the high Mn and Al contents in low-density steel, solid reactions between oxide inclusions and Al in low-density steel are inevitable. Fundamental studies on the interactions between oxide inclusions and low-density steel during heat treatment are scarce.

Generally, diffusion couple method was used to observe the interaction between the NMIs and steel matrix during the heat treatment. According to the literatures,[13–21] several methods are available to prepare diffusion couple specimens. Wang *et al.*[21] prepared diffusion couples by clamping the oxide powder between two steel cylinders and then sealed the diffusion couple in a quartz tube. Kim *et al.*[13,14] smelted oxides and steel in a SiO_2 crucible under a CO/CO_2 atmosphere at 1823 K (1600 °C) and then quenched them in water. Liu *et al.*[15,16] melted oxides on a steel surface at 1673 K (1400 °C) using a confocal scanning laser microscope (CSLM) under an Ar atmosphere and then quenched them immediately. For the clamping method, no preexisting oxide particles were found in the interface. However, the sample preparation process was complicated, and the pressure on the interface might affect the experimental results. For the melting and quenching method, the interfaces were firmly combined but the interaction between oxide and steel was inevitable during process of preparing diffusion couple specimens.

In this study, a novel liquid-metal-suction (LMS) method was performed to prepare diffusion couple specimens. Then, diffusion couple specimens were used to investigate the interactions between the oxide inclusions (Al_2O_3 and MgO) and low-density steel during heat treatment at 1373 K (1100 °C). In addition, the Mn diffusion behavior during heat treatment was also elucidated.

II. EXPERIMENTAL SECTION

A. *Materials and Experimental Methods*

The Al_2O_3/steel and MgO/steel interfaces were investigated after heat treatment. The designed composition of the low-density steel was Fe-12Mn-1Al-0.7C (wt pct). The raw materials were industrial pure iron (99.8 wt pct), electrolytic manganese (99.9 wt pct), aluminum particles (99.9 wt pct), and graphite blocks (99.9 wt pct). The oxide rods were high purity Al_2O_3 (99.9 wt pct) and MgO (99.9 wt pct).

In the steel-smelting process, the industrial pure iron and graphite blocks were first placed in a corundum crucible, and a mixed gas (Ar-5 vol pct H_2) was introduced into the furnace at a flow rate of 0.5 L/min for 5 hours. Then, the resistance furnace was heated. When the temperature approached 1873 K (1600 °C), electrolytic manganese and aluminum particles were added to molten steel. The molten steel was held at 1873 K (1600 °C) for 10 min to homogenize the composition.

To obtain a good interface between the oxide rod and steel, a liquid-metal-suction (LMS) method was performed to prepare the diffusion couple specimens, as shown in Figure 1. The LMS method was reported by Wang *et al.*[22] to study the early stage of the dissolution behavior of FeCr alloy in liquid iron. A quartz tube (6 mm inner diameter) was pre-shrunken and then preloaded with an oxide rod. After the homogenization of molten steel, the diffusion couple specimens were obtained using a quartz tube. The obtained specimen was cut into two pieces. One part was used to observe the original oxide/steel interface before heat treatment, and the other part was used to prepare the diffusion couple specimen.

The diffusion couple specimen was sealed in a quartz tube (12 mm inner diameter) filled with a gas mixture (Ar-5 vol pct H_2) at a pressure of approximately 2×10^4 Pa after vacuum pumping. Then, the quartz tube was transferred to a muffle furnace and subjected to heat treatment at 1373 K (1100 °C) for 10 h.

B. *Analysis of Specimens*

The diffusion couple specimens were ground with 400, 800, 1200, and 2000 grit SiC papers and then mirror polished with a 1 μm diamond suspension. The oxide/steel interfaces were analyzed using an electron probe microanalyzer (EPMA) and scanning electron microscopy (SEM) with energy-dispersive spectroscopy (EDS). The accelerating voltage for EPMA analysis was 15 kV, and the beam current was 0.1 μA. Moreover,

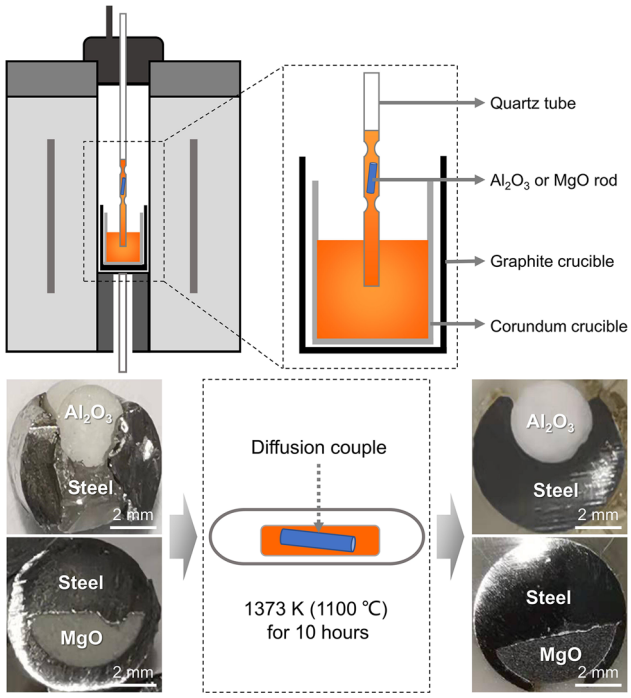

Fig. 1—Experimental procedure for the preparation of the diffusion couple specimens.

the morphology and chemical composition of NMIs in steel were detected by SEM and EDS. The number of NMIs was statistically analyzed based on 50 random images (×500 magnification), which were obtained by SEM. Additionally, only NMIs over 0.5 μm were considered.

III. RESULTS

A. *Non-metallic Inclusions in the Steel Matrix*

Based on the observation and detection of Al_2O_3/steel and MgO/steel diffusion couple specimens, there were few differences in the types of NMIs in the low-density steel matrix (far from the oxide/steel interface). However, the heat treatment had a significant influence on the morphology and number of NMIs. Figure 2 shows the typical NMIs in the steel matrix before and after the heat treatment.

Before heat treatment, the main NMIs in the steel matrix were AlN, MnS, AlN–MnS, and a small amount of Al_2O_3–MnS, as shown in Figures 2(a) through (d). Generally, the pure AlN particles had a polygonal structure, and some agglomerated AlN inclusions were also detected. The MnS inclusion was irregular with a size of approximately 4 μm. In addition, the detected AlN–MnS and Al_2O_3–MnS complex inclusions are commonly irregular shapes, and the AlN and Al_2O_3 particles are completely wrapped with MnS.

After the heat treatment was performed at 1373 K (1100 °C) for 10 hours, there were no obvious differences in the types of inclusions in the steel matrix (Figures 2(e) through (h)). AlN, MnS, and AlN–MnS were still the dominant inclusions in the steel matrix, and the AlN inclusions remained in the polygonal structure. The morphologies of the MnS and AlN–MnS became spherical or near-spherical, which was consistent with the observation in the relevant literatures.[23–25] The main reason was that the chemical potential of curved surfaces was higher than that of flat surfaces in the MnS inclusions, which then led to the surface diffusion of Mn and S atoms.

The relative fractions of typical NMIs in the steel matrix before and after heat treatment were also statistically analyzed, as shown in Figure 3. The considered NMIs were classified as AlN, AlN–MnS, MnS, and others (Al_2O_3, Al_2O_3–MnS, Al_2O_3–AlN, Al_2O_3–AlN–MnS). The fraction value of pure AlN inclusions increased from 43 to 78 pct after heat treatment. Before heat treatment, the fraction values of AlN–MnS, pure MnS, and other inclusions were 27, 17, and 13 pct, respectively. However, those values correspondingly decreased to 11, 4, and 7 pct after heat treatment. The main reason for the increase in the number of AlN inclusions was the precipitation of a large number of fine AlN particles during heat treatment, which is consistent with the reports by Lu[26] and Alcântara. [27] Due to the dissolution of the MnS inclusions during heat treatment, the fraction values of MnS-containing inclusions decreased.

B. *Interface Between Al_2O_3 and Steel*

The Al_2O_3/steel interface was observed using EPMA, and the morphology of the interface and the element mappings of Fe, Mn, Al, and O before heat treatment are shown in Figure 4. The Al_2O_3 rod and steel were tightly combined. The dark phase is bulk Al_2O_3, and the light gray phase is the low-density steel matrix. Some particles were detected in the steel matrix, which were AlN, MnS, and the related inclusions, as mentioned earlier. Near the interface on the steel side, oxygen was not detected, which indicated that there was virtually no diffusion of oxygen from the bulk Al_2O_3 to the steel matrix during the sampling process. Moreover, Mn enrichment phenomenon was observed near the Al_2O_3/steel interface mainly because of the microsegregation of solutes during specimen solidification.

Figure 5 shows the morphology and element mappings of the Al_2O_3/steel interface after heat treatment at 1373 K (1100 °C) for 10 h. Based on the EPMA analysis, many particles composed of Al and O were observed. These Al_2O_3 particles were neatly distributed on the steel matrix side near the interface, and the size of the particles was starkly polarized. The coarse Al_2O_3 particles with sizes ranging from 5 to 10 μm were

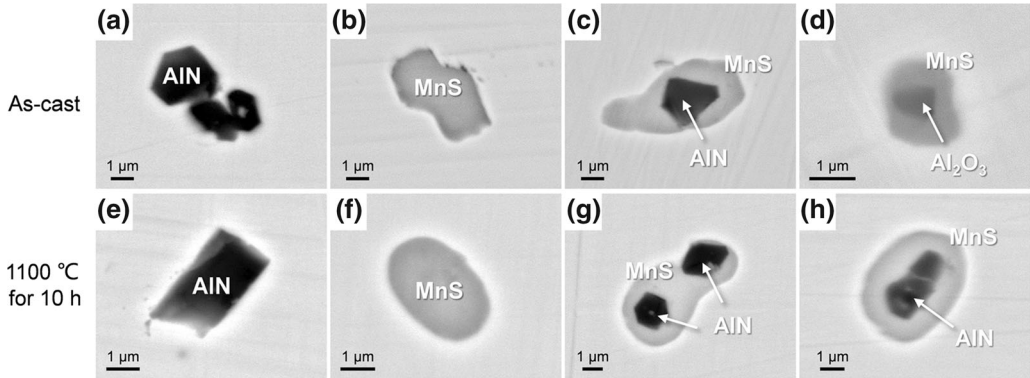

Fig. 2—Typical morphology and composition of NMIs in the low-density steel. (*a*) through (*d*) before heat treatment; (*e*) through (*h*) after heat treatment at 1373 K (1100 °C) for 10 h.

approximately vertical to the Al_2O_3/steel interface. It was concluded that there was a trend of growth toward the steel matrix during heat treatment. The fine Al_2O_3 particles with nanoscale sizes were mainly concentrated near the Al_2O_3/steel interface.

The oxide particle zone in the steel matrix near the interface is commonly defined as the particle precipitation zone (PPZ). The average width of the PPZ (including coarse Al_2O_3 particles and fine Al_2O_3 particles) near the Al_2O_3/steel interface was 9.3 μm.

Notably, an essentially pure metal surface layer between PPZ and the interface was observed. The formation mechanism was that the molar volume of oxide particles formed in the steel matrix was larger than that of the alloy matrix.[28,29] This discrepancy resulted in a gradient of internal stress between the internal oxide front (IOF) and the stress-free surface, and the driving force from internal stress caused the steel matrix to ooze out to form a nearly pure surface layer.

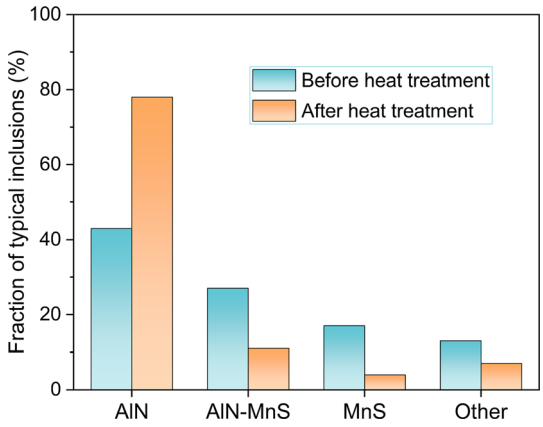

Fig. 3—Relative fractions of typical NMIs in the low-density steel matrix.

C. *Interface Between MgO and Steel*

Figure 6 shows the morphology and mappings of Fe, Mn, Mg, Al, and O at the MgO/steel interface before heat treatment. The interface between the MgO rod and steel is visible. A small amount of discontinuous $MgO{\cdot}Al_2O_3$ (MA) spinel was detected on the bulk MgO side, where the Al content was higher. This observation may be due to the rapid chemical reaction between the Al from molten steel and the MgO rod during the sampling process. The reaction between Al and MgO in low-density steel at 1873 K (1600 °C) has been reported elsewhere.[10]

Figure 7 shows the interfacial characteristics between the MgO rod and low-density steel after heat treatment. An MA spinel layer (part I) was observed on the bulk MgO side near the interface, with a width from 2 to 5 μm. On the steel side, discontinuous MA spinel particles (part II) and dendritic Al_2O_3 (part III) were observed near the MgO/steel interface. The size of dendritic Al_2O_3 was up to 20.0 μm, which also tended to extend into the steel matrix. As shown in the EPMA images, the PPZ was composed of part II and part III, which were approximately 30.0 μm wide in the steel matrix. Notably, there was a clear concentration gradient of Mn from the interior to the surface of the steel matrix according to the element mapping of Mn. The Mn content on the surface of the steel matrix was obviously lower than that in the inner part.

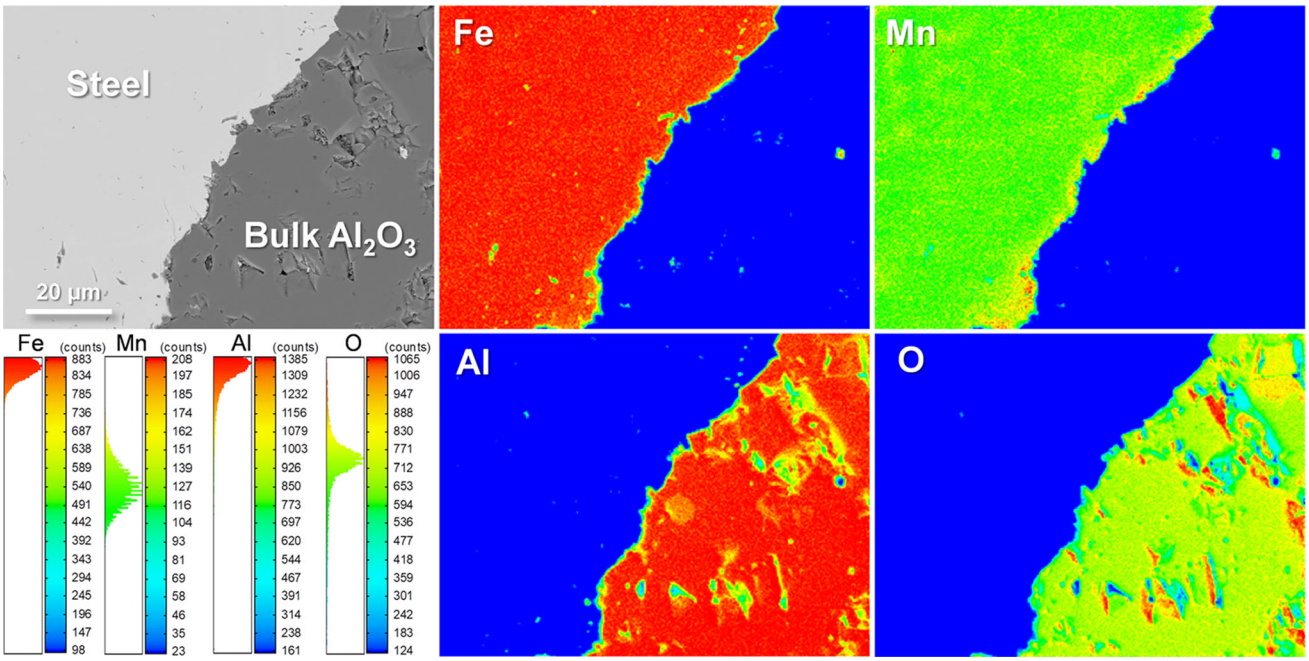

Fig. 4—EPMA images of the Al_2O_3/steel interface before heat treatment.

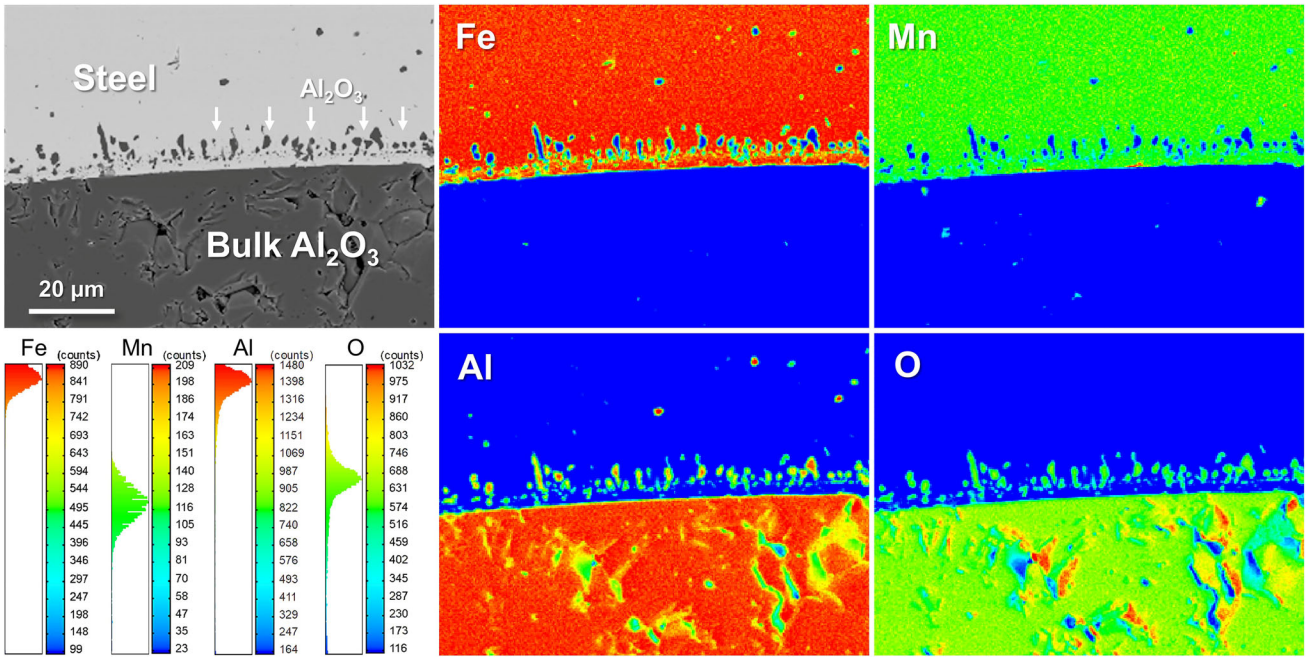

Fig. 5—EPMA images of the Al_2O_3/steel interface after heat treatment.

D. *Distribution of Elements Near the Oxide/Steel Interface*

Based on the results of the EPMA detection, a rectangular region vertical to the oxide/steel interface was selected to reveal the changes in Mn, Al, and Mg content before and after heat treatment, and the changes in the contents of the related elements near the oxide/steel interface are shown in Figure 8. At the Al_2O_3/steel interface before heat treatment, the Al content remained at approximately 1 wt pct, whereas the Mn content fluctuated due to microscopic segregation in the steel matrix.[30] After heat treatment, the PPZ with Al_2O_3 particles was formed in the Al_2O_3/steel interface. In the PPZ, the Mn content gradually decreased from 11 to 8 wt pct, and the Al content correspondingly increased from 1 to 5 wt pct. An Al-depleted zone (ADZ) was observed in the steel matrix because the formation of Al_2O_3 particles in PPZ consumed Al in the steel matrix.

The changes in Mn, Al, and Mg contents near the MgO/steel interface before and after heat treatment are shown in Figure 8(b). Before heat treatment, the Al content was approximately stable at 1 wt pct in the steel matrix, and no Mg was detected. The Mn content fluctuated at approximately 12 wt pct, and the peak of Mn content may be due to microscopic segregation or the formation of MnS inclusions in the steel matrix.

After heat treatment, a PPZ composed of MA spinel and Al_2O_3 particles was observed on the steel side, which led to a decrease in Mn content. The peaks of Al and Mg corresponded to the MA spinel particle, and the nearby high Al content (no Mg) corresponded to the Al_2O_3 particle. As mentioned earlier, the formation of Al_2O_3 particles led to an ADZ in the steel matrix after heat treatment. The Mn content decreased from the steel matrix to the MgO/steel interface, which reflected that Mn diffusion occurred during the heating.

In summary, the contents of Mn, Al, and Mg were stable from the interior to the surface of the steel matrix before heat treatment. After heat treatment, Al_2O_3 particles were formed in the PPZ for the Al_2O_3/steel interface, and MA spinel and Al_2O_3 particles were formed in the PPZ for the MgO/steel interface. The formation of related oxide particles caused an ADZ in the steel matrix. Mn diffusion was subsequently observed due to the heat treatment.

IV. DISCUSSION

A. *Mn Diffusion Behavior*

The variation in Mn content vertical to the interface in low-density steel was obvious after heating at 1373 K (1100 °C) for 10 hours. Generally, there are three reasons for Mn variation in steel. One is the evaporation of Mn during heat treatment, the second is the formation of Mn-containing oxide particles, which consume Mn in the steel matrix, and the third is the Mn diffusion behavior during the heating process.

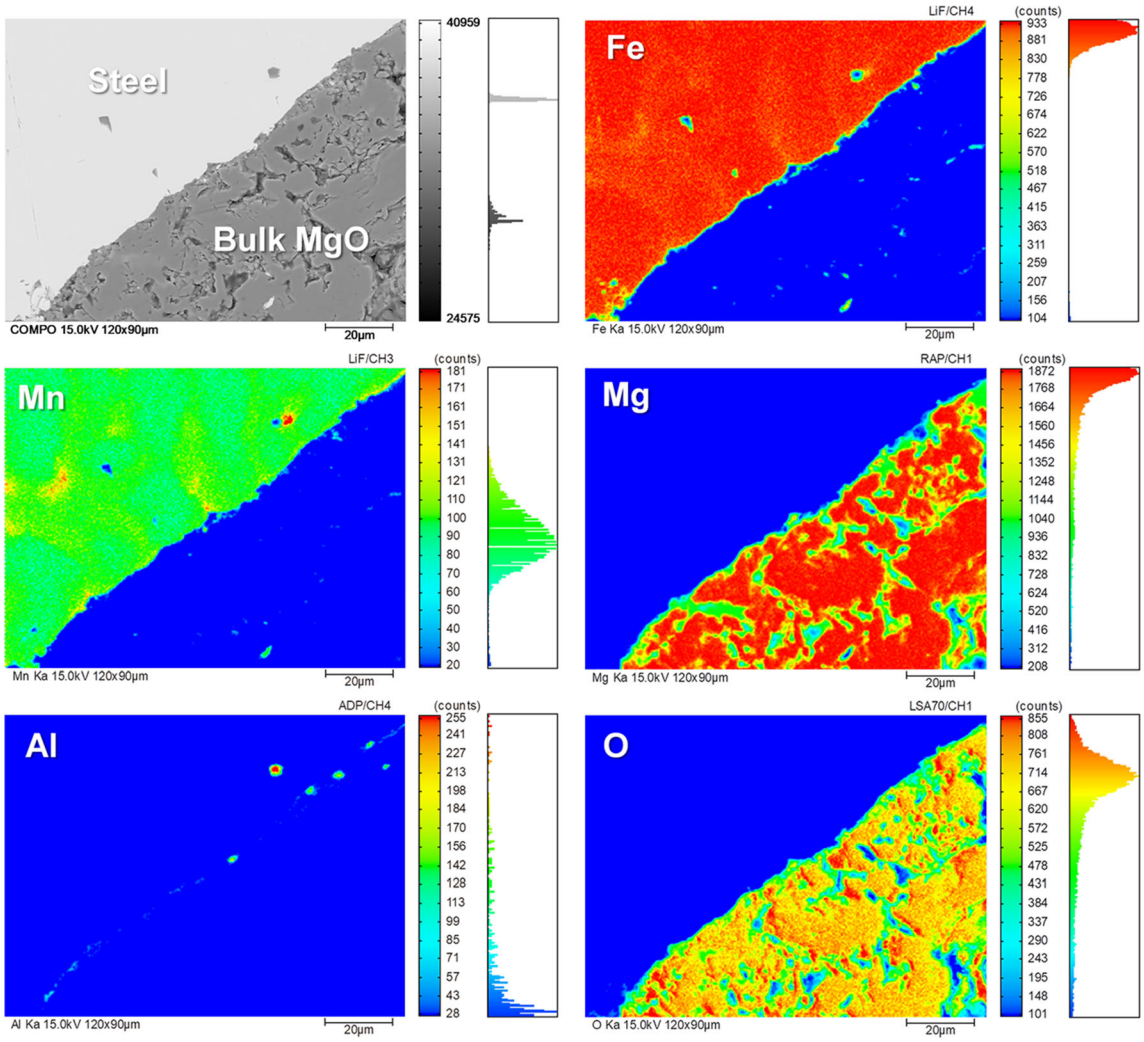

Fig. 6—EPMA images of the MgO/steel interface before heat treatment.

Jimbert and Tomota *et al.*[31,32] confirmed that Mn and Cr could cause heterogeneities in steel because of metal evaporation at heating temperatures above 1273 K (1000 °C). Liu *et al.* and Kim *et al.*[14–16] reported that the decrease in Mn content in the Mn-depleted zone (MDZ) was due to the solid reaction between oxygen from the interface and Mn and Si in the steel matrix, and then MnO–SiO_2 particles formed in the PPZ. In this study, no Mn-containing oxide particles were detected in the PPZ, and Mn did not participate in the solid reaction at the oxide/steel interface. Moreover, the direction of Mn variation was perpendicular to the oxide/steel interface. The main reason for the decrease in Mn content from the inner steel matrix to the interface was Mn diffusion.

To understand the Mn diffusion behavior during heat treatment, a theoretical calculation was performed based on Fick's second law. The calculation was made under the following assumptions[32]:

1. Mn evaporation occurs instantaneously from the outermost atomic layer of the MgO/steel interface during heating;
2. The kinetics of Mn evaporation are controlled by the diffusivity of Mn in the steel matrix;
3. Mn diffusivity is independent of its content and determined by the impurity diffusion coefficient;
4. The Mn content at the interface always remains constant at zero.

Considering that Mn diffusion is one-dimensional, Fick's second law can be written as follows:

$$\frac{\partial C}{\partial t} = D\frac{\partial^2 C}{\partial x^2}, \qquad [1]$$

where C is the Mn content, D is the diffusion coefficient, t is the heating time, and x is the distance from the interface. Then, Equation [1] can be transformed into a finite difference expression, as shown in Eq. [2].

$$C_x^{t+\Delta t} = C_x^t + D\frac{\Delta t}{\Delta x^2}\left(C_{x+\Delta x}^t - 2C_x^t + C_{x-\Delta x}^t\right), \qquad [2]$$

where C_x^t represents the Mn content at distance x and time t, and the diffusion coefficient D is determined by the Arrhenius equation, as shown in Eq. [3].

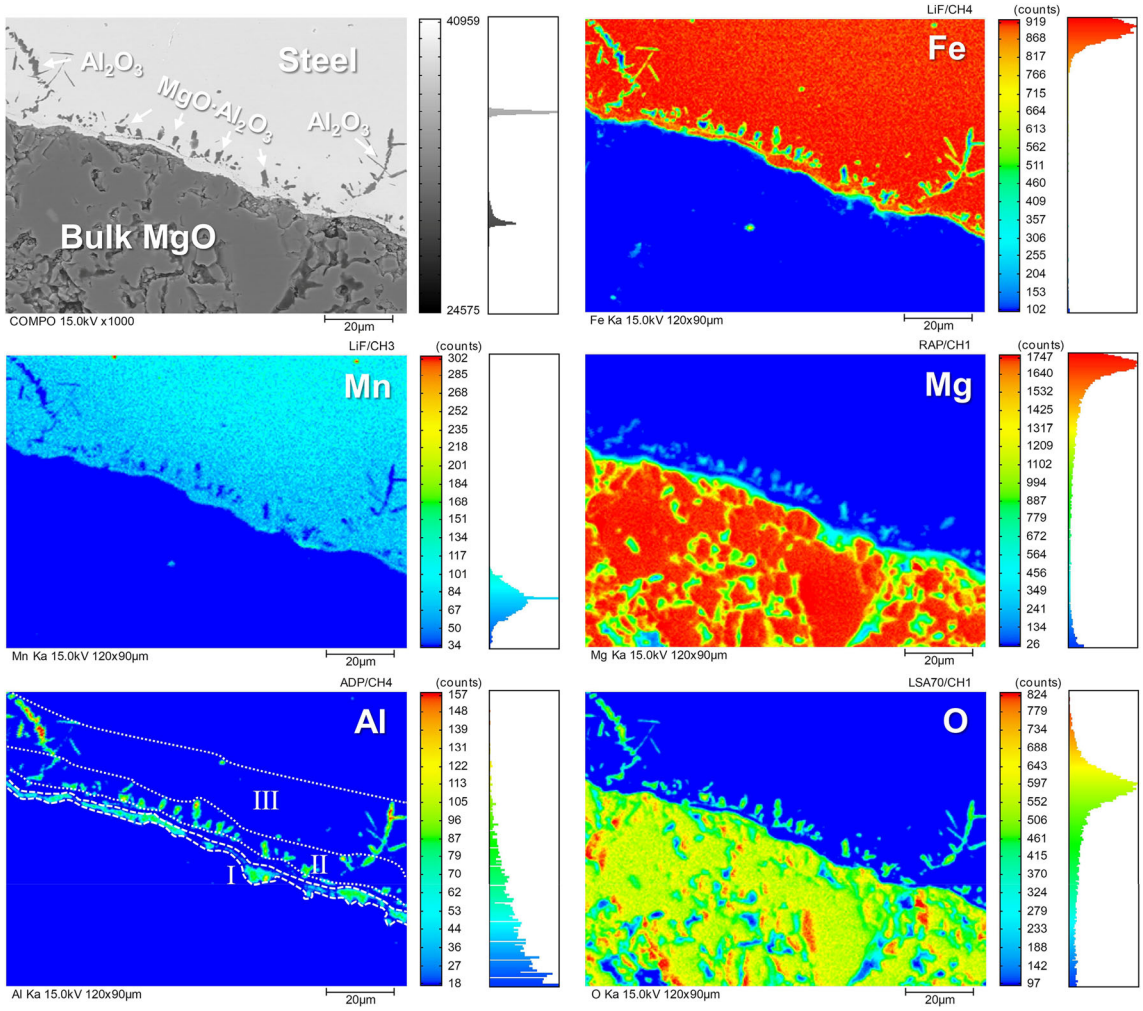

Fig. 7—EPMA images of the MgO/steel interface after heat treatment.

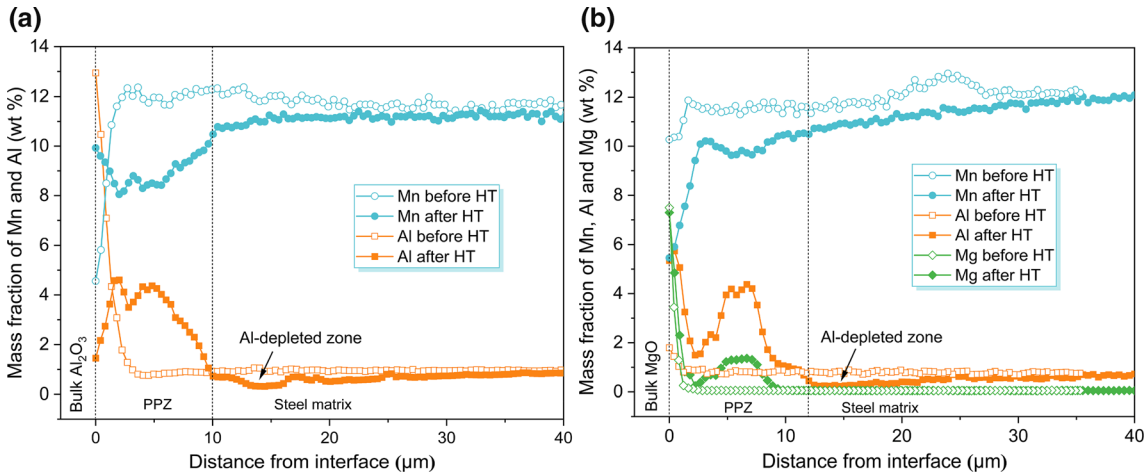

Fig. 8—Changes in Mn, Al and Mg contents near the Al_2O_3/steel (*a*) and MgO/steel (*b*) interfaces.

$$D = D_0 exp\left(-\frac{Q}{RT}\right), \quad [3]$$

where Q is the activation energy, D_0 is the preexponential factor, R is the gas constant, and T is the heating temperature. Therefore, the finite difference expression can be written as the following equation.

$$C_x^{t+\Delta t} = C_x^t + \left(C_{x+\Delta x}^t - 2C_x^t + C_{x-\Delta x}^t\right)\frac{\Delta t}{\Delta x^2} D_0 exp\left(-\frac{Q}{RT}\right) \quad [4]$$

The related data used for these calculations are as follows:

The Mn content in the steel matrix is 12 wt pct, the heating temperature is 1373 K (1100 °C), the gas constant R = 8.31 J/(mol·K), the preexponential factor D_0 = 5.01×10^{-4} m^2/s, and the activation energy for diffusion Q = 288.4 kJ/mol. The D_0 and Q used here are from the literature.[33] Moreover, the calculation was performed with segment sizes of Δx = 1 μm and Δt = 10 s.

The theoretical relationships among the variation in Mn content, heating time, and the distance from the interface are plotted in Figure 9. The Mn contents decreased obviously with decreasing distance from the interface. The closer to the interface, the higher the rate of Mn reduction. The region with a Mn content ranging from 11.88 wt pct (0.99 × original Mn content) to zero can be defined as an Mn-depleted zone (MDZ). In the MDZ, a longer heat treatment time resulted in a lower Mn content at the same distance from the interface. The Mn diffusion area was associated with the heating time, and the MDZ widths were 16, 28, 36, 44, and 50 μm, corresponding to heating times of 1, 3, 5, 8, and 10 hours, respectively. It can be concluded that the Mn content in the steel matrix was significantly influenced by the heating time and the distance from the interface.

The theoretically calculated MDZ width was approximately 50 μm with heat treatment at 1373 K (1100 °C) for 10 h, which was larger than the observation in the current study (approximately 40 μm). One reason was that the bulk MgO inhibited the Mn evaporating from the MgO/steel interface and consequently weakened the Mn diffusion from the steel matrix. The other reason was that the Mn content in the oxide/steel interface was set to zero.

The Mn content in the interface after heat treatment, as shown in Figure 8(b), indicates that the Mn content from the inner steel matrix and the interface was considered to range from 12 to 9 wt pct. The theoretical Mn content in the steel matrix was recalculated, and the relationship between the Mn content and distance from the interface after heat treatment at 1373 K (1100 °C) for 10 h is shown in Figure 10. The Mn contents detected during EPMA analysis are also superimposed in Figure 10. It can be seen that Mn began to diffuse approximately 40 μm from the interface. This experimental observation was consistent with the calculation.

B. *Solid Reaction Between Oxide and Steel*

To observe the details of the Al_2O_3/steel interface after heat treatment, the interface was observed using SEM and EDS. Figure 11 shows the details of the interface and the line scanning of the oxide particles. As mentioned earlier, there were two types of Al_2O_3 particles. Some were fine Al_2O_3 particles with a width of approximately 2.0 μm, and the others were coarse Al_2O_3 particles with an average width of 9.3 μm. In addition, the coarse Al_2O_3 particles tended to grow into the steel matrix as the heat treatment proceeded.

Based on the ion and molecule coexistence theory, Al_2O_3 are complex macromolecules that consist of and coexist with simple molecules and simple ion pairs.[34] Solid Al_2O_3 exists in the ionic state of Al^{3+} and O^{2-}, and heat treatment at temperatures ranging from 1300 K to 1700 K resulted in a loss of oxygen from the surface.[35,36] Due to the concentration gradient of oxygen between the bulk Al_2O_3 and the steel matrix, the formation of the PPZ can be concluded as shown in Figure 12. First, Al^{3+} and O^{2-} diffused through the interface from the bulk Al_2O_3 under the condition of

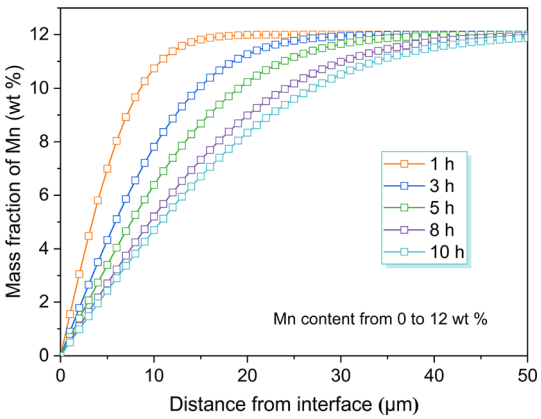

Fig. 9—Change in Mn content at different heating times.

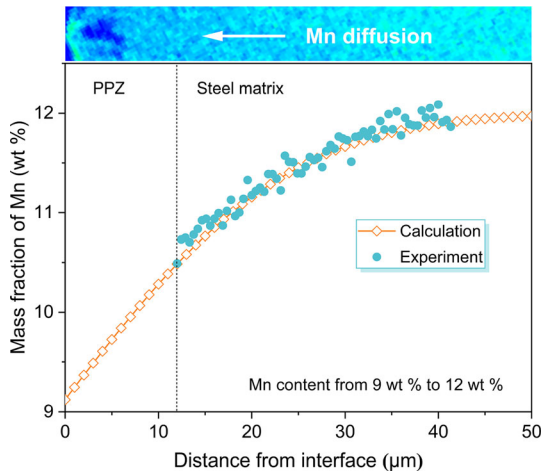

Fig. 10—Distribution of Mn after heat treatment at 1373 K (1100 °C) for 10 h.

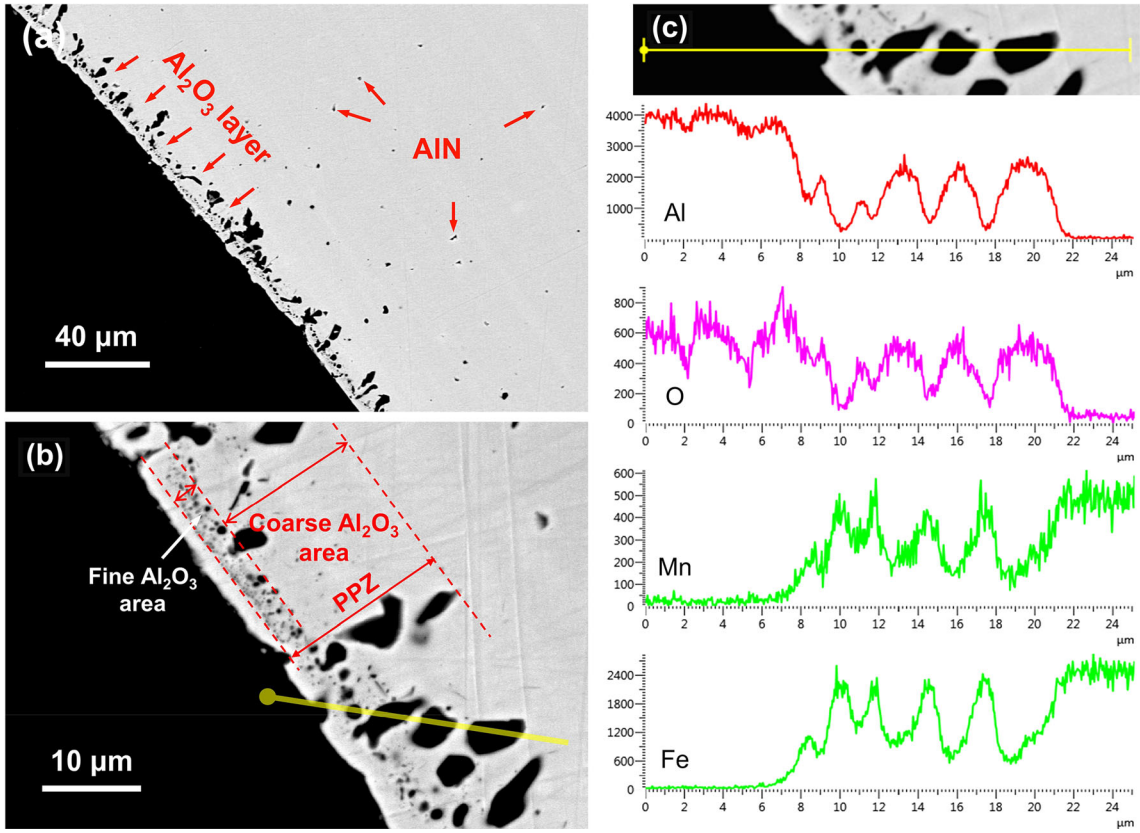

Fig. 11—Interface between Al_2O_3 and low-density steel after heat treatment. (*a*) 500× magnification; (*b*) 2000× magnification; (*c*) EDS line scanning.

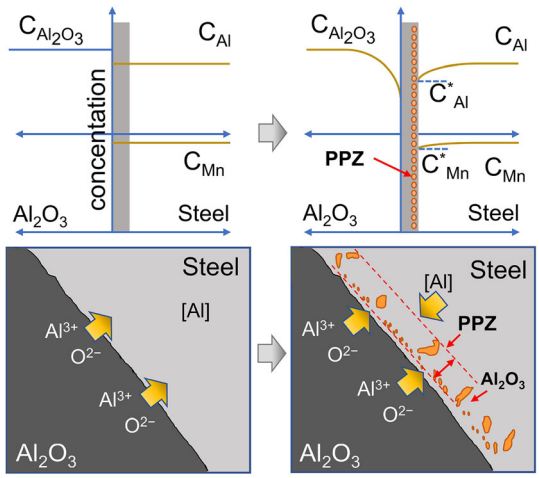

Fig. 12—Formation mechanism of the PPZ in the Al_2O_3/steel interface.

electrical neutrality. As the concentration of Al and O increased on the steel side, Al_2O_3 particles formed, and the solid reaction equation is shown in Eq. [5].[37–39]

$$2[Al] + 3[O] = Al_2O_{3(s)} \quad \log K_1 = 64000/T - 20.48 \quad [5]$$

The diffusion of [O] was faster than that of [Al] in the process of [Al] and [O] diffusion from the interface to the steel matrix.[14,16] This observation indicates that the formation of Al_2O_3 particles consumed aluminum from the steel matrix, leading to an ADZ in the steel matrix near the PPZ. As the heat treatment proceeded, the Al_2O_3 particles grew, fine Al_2O_3 particles were transformed into coarse Al_2O_3 particles, and then the coarse Al_2O_3 particles extended into the steel matrix.

Figure 13 shows the morphologies of the PPZ at the MgO/steel interface. After heat treatment at 1373 K (1100 °C) for 10 hours, three oxide layers were observed in the interface. A thin MA spinel layer was formed on the bulk MgO side, and MA spinel particles were generated on the steel side. The line scanning of the oxide shows that the dendritic oxide was composed of MA spinel and coarse Al_2O_3. The large-sized dendritic Al_2O_3 tended to extend into the steel matrix. The average width of the MA spinel particles was 8.0 μm. The PPZ (approximately 30 μm) included MA spinel particles and Al_2O_3.

MgO is a highly ionic crystalline solid with a rock-salt crystal structure. Solid MgO has fcc Mg^+ and O^- sublattices. [40,41] It can be inferred that Mg^{2+} and O^{2-} are present in bulk MgO during heat treatment, and the equilibrium equation is shown in Eq. [6].[37–39] For the

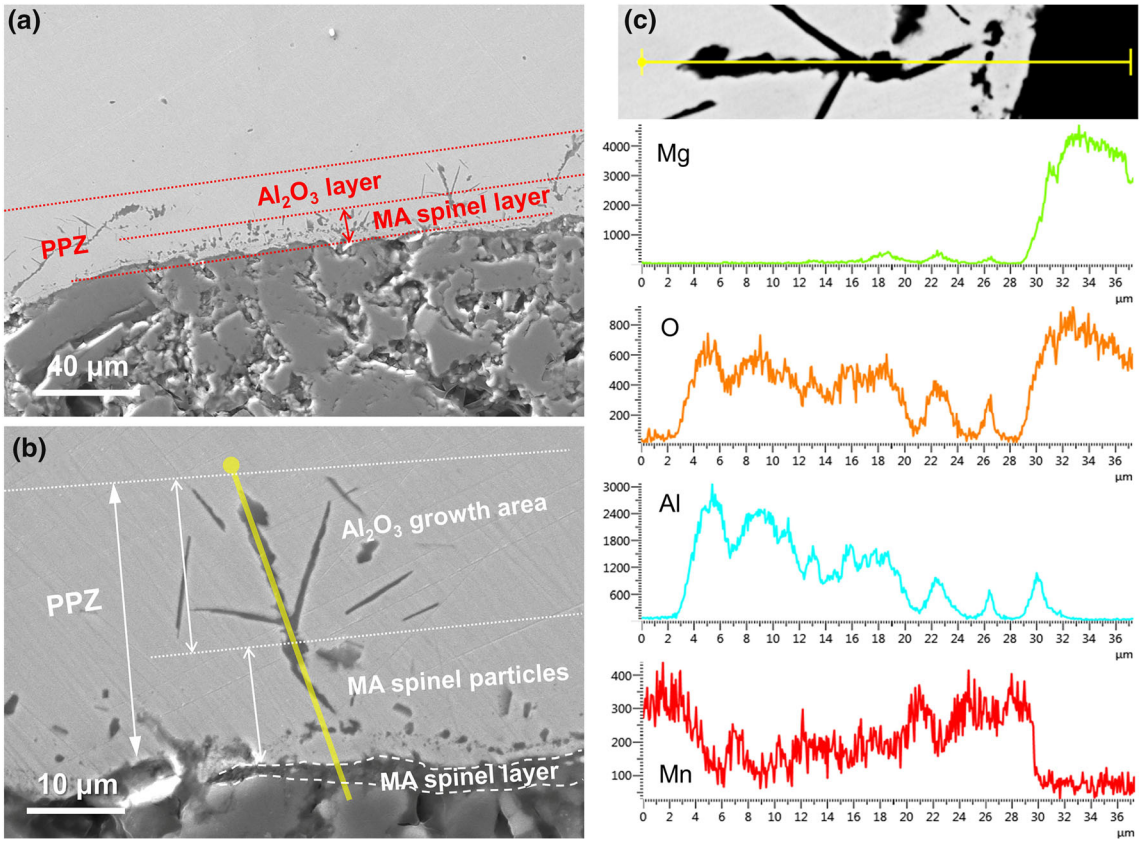

Fig. 13—Interface between MgO and low-density steel after heat treatment. (*a*) 500× magnification; (*b*) 2000× magnification; (*c*) EDS line scanning.

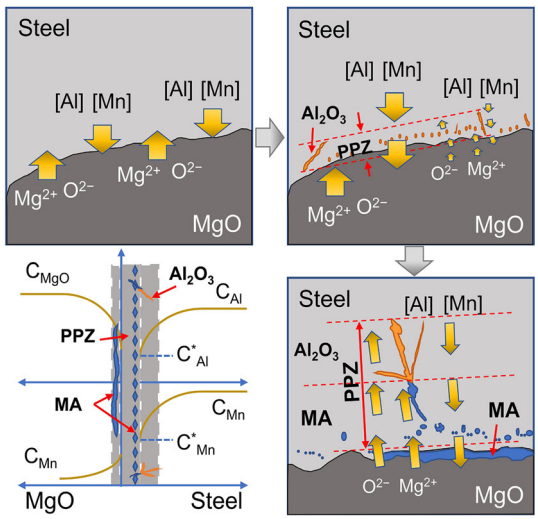

Fig. 14—Formation mechanism of the PPZ in the MgO/steel interface.

MgO/steel interface, the formation of PPZ and the solid reaction can be concluded, as shown in Figure 14. As the heat treatment proceeds, Mg^{2+} and O^{2-} diffuse through the interface from the bulk MgO, while [Al] and [Mn] diffuse to the interface from the steel matrix. With the increase in Al concentration on the bulk MgO side, a thin MA spinel with a strip shape was formed due to the solid reaction, as shown in Eqs. [7] and [8].[39]

$$MgO_{(s)} = [Mg] + [O] \quad \log K_2 = -38059/T + 12.45 \quad [6]$$

$$2[Al] + [Mg] + 4[O] = MgO \cdot Al_2O_{3(s)} \quad \log K_3 = 51080/T - 6.736 \quad [7]$$

$$2[Al] + 4MgO_{(s)} = MgO \cdot Al_2O_{3(s)} + 3[Mg] \quad \log K_4 = 32280/T - 23.856 \quad [8]$$

$$3[Mg] + 4Al_2O_{3(s)} = 3MgO \cdot Al_2O_{3(s)} + 2[Al] \quad \log K_5 = -27950/T + 26.274 \quad [9]$$

With the diffusion of [O] from the bulk MgO to the steel matrix, [O] reacted with [Al] to form Al_2O_3 particles on the steel side. Subsequently, those Al_2O_3 particles were transferred to MA spinel particles according to Eq. [9].[42,43] Since the diffusion of [O] was faster than that of [Mg] in the steel matrix, the Al_2O_3 particle area was larger than that of MA spinel.[14,16] It can be

inferred that the PPZ continuously expanded to the interior of the steel matrix as the heat treatment proceeded.

V. CONCLUSIONS

In the current study, a novel LMS method was performed to prepare diffusion couple specimens, and the Al_2O_3/steel and MgO/steel interfaces after heat treatment at 1373 K (1100 °C) were observed. The typical NMIs and Mn diffusion behavior were also revealed, and the following conclusions were obtained:

(1) Before heat treatment, the main NMIs in the low-density steel matrix were AlN, MnS, AlN–MnS, and a small number of Al_2O_3–MnS. After heat treatment, there were no obvious differences in the types of NMIs, whereas MnS and AlN–MnS became spherical or nearly spherical, and the number of fine AlN inclusions increased.
(2) After heat treatment, the oxide particles in the PPZ were fine Al_2O_3 and coarse Al_2O_3 at the Al_2O_3/steel interface. At the MgO/steel interface, three oxide layers were observed near the interface. A thin MA spinel layer was formed on the bulk MgO side, and the MA spinel particles and dendritic Al_2O_3 constituted the PPZ on the steel side. The formation of oxide particles in the PPZ was mainly due to oxygen diffusion from the bulk oxides to the steel.
(3) The formation of Al_2O_3 particles in the PPZ led to an Al-depleted zone in the steel matrix. The variation in Mn content vertical to the interface in low-density steel was obvious due to Mn diffusion. Based on Fick's second law, Mn diffusion was significantly influenced by heating time and temperature. The detected Mn contents from EPMA analysis after heat treatment were consistent with the calculation.

ACKNOWLEDGMENTS

This work was supported by the National Natural Science Foundation of China (Grant No. 52074199).

CONFLICT OF INTEREST

The authors declare that they have no known competing financial interests or personal relationships that could have appeared to influence the work reported in this paper.

REFERENCES

1. I. Gutierrez-Urrutia: *ISIJ Int*., 2021, vol. 61, pp. 16–25. https://doi.org/10.2355/isijinternational.ISIJINT-2020-467.
2. S. Chen, R. Rana, A. Haldar, and R.K. Ray: *Prog. Mater. Sci*., 2017, vol. 89, pp. 345–91. https://doi.org/10.1016/j.pmatsci.2017.05.002.
3. D.W. Suh and N.J. Kim: *Scr. Mater*., 2013, vol. 68, pp. 337–38. https://doi.org/10.1016/j.scriptamat.2012.11.037.
4. H. Tervo, A. Kaijalainen, T. Pikkarainen, S. Mehtonen, and D. Porter: *Mater. Sci. Eng. A*, 2017, vol. 697, pp. 184–93. https://doi.org/10.1016/j.msea.2017.05.013.
5. R. VazPenna, L.N. Bartlett, and T. Constance: *Int. J. Metalcast*., 2019, vol. 13, pp. 286–99. https://doi.org/10.1007/s40962-018-0273-9s.
6. H. Suito and R. Inoue: *ISIJ Int*., 1996, vol. 36, pp. 528–36. https://doi.org/10.2355/isijinternational.36.528.
7. M. Nabeel, M. Alba, A. Karasev, P.G. Jönsson, and N. Dogan: *Metall. Mater. Trans. B*, 2019, vol. 50, pp. 1674–85. https://doi.org/10.1007/s11663-019-01605-0.
8. W. Wang, H. Zhu, Y. Han, J. Li, and Z. Xue: *Steelmak*, 2021, vol. 48, pp. 1038–47. https://doi.org/10.1080/03019233.2021.1909993.
9. D.J. Kim and J.H. Park: *Metall. Mater. Trans. B*, 2012, vol. 43, pp. 875–86. https://doi.org/10.1007/s11663-012-9667-x.
10. L. Wang, H. Zhu, J. Zhao, J. Li, and Z. Xue: *Ceram. Int*., 2022, vol. 48, pp. 1090–97. https://doi.org/10.1016/j.ceramint.2021.09.194.
11. Y. Ren, L. Zhang, and P.C. Pistorius: *Metall. Mater. Trans. B*, 2017, vol. 48, pp. 2281–92. https://doi.org/10.1007/s11663-017-1007-8.
12. W. Yang, S. Liu, S. Han, J. Wang, J. Guo, Y. Yan, and H. Guo: *Materials*, 2020, vol. 13, p. 5396. https://doi.org/10.3390/ma13235396.
13. K.H. Kim, S.J. Kim, H. Shibata, and S. Kitamura: *ISIJ Int*., 2014, vol. 54, pp. 2144–53. https://doi.org/10.2355/isijinternational.54.2144.
14. K.H. Kim, H. Shibata, and S. Kitamura: *ISIJ Int*., 2014, vol. 54, pp. 2678–86. https://doi.org/10.2355/isijinternational.54.2678.
15. C. Liu, S. Yang, K.H. Kim, J. Li, H. Shibata, and S. Kitamura: *Int. J. Miner. Metall. Mater*., 2015, vol. 22, pp. 811–19. https://doi.org/10.1007/s12613-015-1138-3.
16. C. Liu, K.H. Kim, S.J. Kim, J. Li, S. Ueda, X. Gao, H. Shibata, and S.Y. Kitamura: *Metall. Materi. Trans. B*, 2015, vol. 46, pp. 1875–84. https://doi.org/10.1007/s11663-015-0356-4.
17. X. Zhang, S. Yang, C. Liu, J. Li, Q. Liu, and G. Liu: *J. Iron Steel Res. Int*., 2018, vol. 25, pp. 1–8. https://doi.org/10.1007/s42243-017-0005-z.
18. S.J. Kim, H. Tago, K.H. Kim, S. Kitamura, and H. Shibata: *Metall. Mater. Trans. B*, 2018, vol. 49, pp. 977–87. https://doi.org/10.1007/s11663-018-1233-8.
19. W. Gan, C. Liu, K. Liao, H. Zhang, and H. Ni: *Metall. Mater. Trans. B*, 2022, vol. 53, pp. 485–502. https://doi.org/10.1007/s11663-021-02385-2.
20. A. Paul and S. Divinski: *Handbook of Solid State Diffusion*: Volume 2. 1st. ed. Oxford: Butterworth-Heinemann; 2017. Chapter 6, Diffusion couple technique: a research tool in materials science, pp. 207–75.
21. Y. Wang, L. Zhang, Y. Ren, H. Duan, and Q. Zhou: *J. Mater. Res. Tech*., 2022, vol. 18, pp. 159–70. https://doi.org/10.1016/j.jmrt.2022.02.084.
22. Y. Wang, A. Karasev, J.H. Park, W. Mu, and P.G. Jönsson: *Metall. Mater. Trans. B*, 2021, vol. 52, pp. 2459–73.
23. Y. Xia, J. Li, H. Dong, Y. Wan, and D. Fan: *Ironmak. Steelmak*., 2021, vol. 48, pp. 222–28. https://doi.org/10.1080/03019233.2020.1833676.
24. X. Shao, X. Wang, M. Jiang, W. Wang, and F. Huang: *ISIJ Int*., 2011, vol. 51, pp. 1995–2001. https://doi.org/10.2355/isijinternational.51.1995.
25. Y.V. Murty, T.Z. Kattamis, R. Mehrabian, and M.C. Flemings: *Metall. Mater. Trans. A*, 1977, vol. 8, pp. 1275–82. https://doi.org/10.1007/BF02643842.
26. P. Lu, H. Li, H. Feng, Z. Jiang, H. Zhu, Z. Liu, and T. He: *Metall. Mater. Trans. B*, 2021, vol. 52, pp. 2210–23. https://doi.org/10.1007/s11663-021-02171-0.
27. F.L. Alcântara, R.A.N.M. Barbosa, and M.A. Cunha: *ISIJ Int*., 2013, vol. 53, pp. 1211–14. https://doi.org/10.2355/isijinternational.53.1211.
28. G. Schimmel, J. Sorina-Müller, B. Kempf, and M. Rettenmayr: *Acta Mater*., 2010, vol. 58, pp. 2091–2102. https://doi.org/10.1016/j.actamat.2009.11.051.
29. S. Guruswamy, S.M. Park, J.P. Hirth, and R.A. Rapp: *Oxid. Met*., 1986, vol. 26, pp. 77–100. https://doi.org/10.1007/BF00664274.

30. Y. Shen, J. Liu, H. Xu, and H. Liu: *Metall. Mater. Trans. B*, 2020, vol. 51, pp. 2963–75. https://doi.org/10.1007/s11663-020-01982-x.
31. P. Jimbert, T. Guraya, I. Kaltzakorta, T. Gutiérrez, R. Elvira, and L.T. Khajavi: *J. Materi. Eng. Perform.*, 2022, vol. 31, pp. 2878–88. https://doi.org/10.1007/s11665-021-06418-4.
32. Y. Tomota, N. Sekido, S. Harjo, T. Kawasaki, W. Gong, and A. Taniyama: *ISIJ Int.*, 2017, vol. 57, pp. 2237–44. https://doi.org/10.2355/isijinternational.ISIJINT-2017-272.
33. K.Y. Tsai, M.H. Tsai, and J.W. Yeh: *Acta Mater.*, 2013, vol. 61, pp. 4887–97. https://doi.org/10.1016/j.actamat.2013.04.058.
34. X. Yang, C. Shi, M. Zhang, G. Chai, and F. Wang: *Metall. Mater. Trans. B*, 2011, vol. 42, pp. 1150–80. https://doi.org/10.1007/s11663-011-9547-9.
35. Z. Luo: *Acta Cryst. B*, 2021, vol. 77, pp. 772–84. https://doi.org/10.1107/S2052520621008027.
36. J. Toofan and P.R. Watson: *Surf. Sci.*, 1998, vol. 401, pp. 162–72. https://doi.org/10.1016/S0039-6028(97)01031-5.
37. L. Yang and G. Cheng: *Int. J. Miner. Metall. Mater.*, 2017, vol. 24, pp. 869–75. https://doi.org/10.1007/s12613-017-1472-8.
38. Z. Deng, Z. Liu, M. Zhu, and L. Huo: *ISIJ Int.*, 2021, vol. 61, pp. 1–5. https://doi.org/10.2355/isijinternational.ISIJINT-2020-352.
39. H. Matsuno and Y. Kikuchi: *Tetsu-to-Hagane*, 2002, vol. 88, pp. 48–50. https://doi.org/10.2355/tetsutohagane1955.88.1_48.
40. A.M.E. Raj, L.C. Nehru, M. Jayachandran, and C. Sanjeeviraja: *Cryst. Res. Tech.*, 2007, vol. 42, pp. 867–75. https://doi.org/10.1002/crat.200710918.
41. A.R. Oganov, M.J. Gillan, and G.D. Price: *J. Chem. Phy.*, 2003, vol. 118, pp. 10174–82. https://doi.org/10.1063/1.1570394.
42. J.H. Park and H. Todoroki: *ISIJ Int.*, 2010, vol. 50, pp. 1333–46. https://doi.org/10.2355/isijinternational.50.1333.
43. V. Brabie: Mechanism of reaction between refractory materials and aluminum deoxidized molten steel. *ISIJ Int.*, 1996, vol. 36, pp. S109-112. https://doi.org/10.2355/isijinternational.36.Suppl_S109.